nature materials

ARTICLES

https://doi.org/10.1038/s41563-017-0003-3

Designing perturbative metamaterials from discrete models

Kathryn H. Matlack[1,2], Marc Serra-Garcia[1*], Antonio Palermo[3], Sebastian D. Huber[2] and Chiara Daraio[1,4]

Identifying material geometries that lead to metamaterials with desired functionalities presents a challenge for the field. Discrete, or reduced-order, models provide a concise description of complex phenomena, such as negative refraction, or topological surface states; therefore, the combination of geometric building blocks to replicate discrete models presenting the desired features represents a promising approach. However, there is no reliable way to solve such an inverse problem. Here, we introduce 'perturbative metamaterials', a class of metamaterials consisting of weakly interacting unit cells. The weak interaction allows us to associate each element of the discrete model with individual geometric features of the metamaterial, thereby enabling a systematic design process. We demonstrate our approach by designing two-dimensional elastic metamaterials that realize Veselago lenses, zero-dispersion bands and topological surface phonons. While our selected examples are within the mechanical domain, the same design principle can be applied to acoustic, thermal and photonic metamaterials composed of weakly interacting unit cells.

Metamaterials utilize subwavelength structures to control wave propagation, achieving extreme functionalities such as focusing beyond the diffraction limit[1–5], performing mathematical operations with light[6] or cloaking objects[7,8]. While the potential of metamaterials is well established, and advanced modelling techniques[9–16] enable the design of some specific functionalities within the electromagnetic domain, we lack systematic approaches to directly encode a generic dynamic functionality into a metamaterial particularly within the mechanical domain. Data-driven design approaches[17–20] have been successful in engineering quasi-static material properties, but extending them to dynamics requires taking into account the interactions between multiple modes of the unit cell. Here, we advocate a systematic approach to design the dynamic properties of a metamaterial.

The key challenge is to bridge the vast design space of possible metamaterial structures and the overwhelming complexity of the targeted physical effect. For example, the phenomenon of the appearance of a topological surface phonon in a mechanical metamaterial cannot be cast into a simple cost function for optimization. However, there are simple discrete models with a small number of parameters that encode this functionality. The key idea of this paper is to use such discrete models as an intermediary between the continuous design space of metamaterial geometries and the targeted functionality (Fig. 1a).

Building systems with complex behaviour from discrete elements is a standard tool in electronics[21–23], where complex devices are designed by combining discrete 'lumped' elements, such as capacitors or inductors. The two challenges we need to overcome, to translate discrete systems into metamaterials, are to identify which metamaterial structures make up which 'lumped' elements, and to quantify how these structures interact with each other. In other words, we need an efficient way to reduce the dynamical behaviour of the material to a discrete model and an efficient way to assess how changes to the design influence the reduced-order model. Identifying the regime where these changes are linear allows us to explore the design space for individual elements and then add their effect. This additive property allows us to divide the search space into much smaller independent subspaces, resulting in an exponential speed-up of the search process.

Here, we successfully address these two challenges with 'perturbative metamaterials': systems consisting of unit cells with a spectrum of linear normal modes that weakly interact with modes of neighbouring unit cells. We obtain reduced-order models for our metamaterial through a method adapted from quantum material science: we use the Schrieffer–Wolff transformation[24,25] to isolate modes in the frequency range of interest. We show that with a suitable series expansion of the Schrieffer–Wolff transformation, we can explore on the order of 10^{40} design configurations, which is impossible to do using optimization methods with current computational power.

Our core design approach includes: mapping the elements of a target mass–spring model to elements in the metamaterial design; the creation of a database of such independent design elements; the combinatorial search of this database; a final refinement correcting for weak nonlinearities (that is, spurious mutual influences of the different geometric elements). These four steps are detailed in numerical design examples of elastic metamaterials comprised of stiff plates connected by soft beams (Fig. 1b). However, the general idea is readily translated to acoustics, optics and so on, if weak coupling of building blocks is achieved (in acoustics, weak coupling can be achieved by small constrictions, whereas in optics this can achieved with tunnel coupled waveguides). We illustrate our method on three examples of increasing complexity.

Extracting a reduced-order model from a metamaterial

In this section, we present a method to extract effective reduced-order models from metamaterials consisting of weakly interacting

[1]Department of Mechanical and Process Engineering, ETH Zürich, Zürich, Switzerland. [2]Institute for Theoretical Physics, ETH Zürich, Zürich, Switzerland. [3]Department of Civil, Chemical, Environmental and Materials Engineering – DICAM, University of Bologna, Bologna, Italy. [4]California Institute of Technology, Pasadena, California, USA. Kathryn H. Matlack and Marc Serra Garcia contributed equally to this work. *e-mail: sermarc@ethz.ch

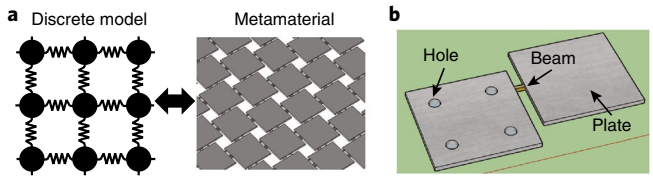

Fig. 1 | Design method concept. a, Design concept of implementing the dynamic functionality of a discrete model in a metamaterial. **b**, Metamaterial design implementation illustrating geometric features: plates, beams and holes.

units, valid over a chosen frequency range of interest. Our selected metamaterial example is in the elastic domain, and contains three basic design elements: vibrational modes of plates, beams that couple the plate modes, and holes that shift local plate frequencies. For applications in other realms, one needs only to replace plates, beams and holes with elements that have resonant modes, and that couple or frequency-shift local modes. The following reduced-order model gives us an efficient way to calculate the coupling and frequency shift of the modes of the metamaterial system, which we refer to as V.

Assume we have two plates that are coupled with a beam (Fig. 1b). The modal discretized displacement field of the two uncoupled plates is defined with the vector $\mathbf{u}$, within a finite-element framework (modelling elasto-dynamics of continuous system). Assuming the beams are short enough that we can consider their effect as instantaneous and neglect their internal degrees of freedom (DOFs), the equation of motion of the coupled plate system can be written as

$$\ddot{\mathbf{u}} + ([M+\Delta M]^{(-1)}[K+\Delta K])\mathbf{u} = 0 \quad (1)$$

where M and K represent the effective mass and stiffness of the plates, and ΔM and ΔK represent the influences of the beams. Under the assumption of weakly interacting unit cells, we can neglect higher powers of ΔK and ΔM, such that

$$\ddot{\mathbf{u}} + (H_0 + V)\mathbf{u} = 0 \quad (2)$$

Here, (H_0+V) is the dynamical matrix of the full coupled system, consisting of $H_0 = M^{-1}K$, the diagonalized dynamical matrix of the uncoupled plates, and $V = M\Delta K - \Delta M K$, the perturbation due to the beams. This perturbation V has two effects: first, it shifts the local mode frequencies and second, it couples each mode of the unit cell to all modes of the same and neighbouring unit cells. The latter prevents us from restricting our description to only modes that lie in our frequency range of interest; that is, H_0+V is not block-diagonal, but instead contains coupling terms between our modes of interest and irrelevant modes. We determine the perturbation, V, from finite-element simulations of systems containing a few plates subjected to this perturbation (for example, Fig. 1b) (Methods, Supplementary Section 1 and Supplementary Fig. 2).

To remove the coupling between relevant and irrelevant spaces, we identify a suitable rotation of the dynamical matrix. This is accomplished by performing a Schrieffer–Wolff transformation (Supplementary Section 1 and Supplementary Fig. 1). Originally developed in the context of the Anderson tight-binding model of magnetic impurities in metals[24], the Schrieffer–Wolff transformation is the rotation matrix R such that $R(H_0+V)R^T$ is block diagonal[25]; that is, it does not present any coupling between modes in the frequency range of interest and other modes. This model reduction is common in condensed-matter physics[26,27], but has never been used to analyse or engineer the dynamical response of metamaterials.

The Schrieffer–Wolff transformation can be calculated perturbatively, with the expansion parameter[25]

$$\epsilon = \frac{V_{ij}}{E_i - E_j} \quad (3)$$

where E_i and E_j are eigenvalues of the uncoupled system, and V_{ij} is the coupling between modes i and j. This expansion parameter can be interpreted as the strength of the coupling relative to the spectral gap between the mode of interest and other modes. For small coupling values, the first-order term provides a satisfactory approximation. This first-order term is linear, which means the effects of the design elements (beams and holes in the plate system) are additive (Supplementary Section 2 and Supplementary Fig. 3). This is of crucial importance later for our design approach. Higher orders of the Schrieffer–Wolff transformation provide a more accurate reduced-order description of the system in the presence of stronger couplings, but contain long-range interactions (that is, stiffness terms that couple plates not physically connected by beams; Supplementary Section 1).

Equipped with an efficient mapping between the metamaterial geometry and reduced-order model, we discuss three examples of the proposed design approach. For illustration purposes, our examples proceed in order of increasing complexity. We start with a negative-refraction Veselago lens, a well-known system that can be realized with conventional metamaterial design techniques (such as, dynamic homogenization of metamaterials with local resonances[28]), but illustrates the correspondence between discrete-model elements and geometric features, and the implementation of positive and negative couplings. We then present a zero-group-velocity metamaterial demonstrating the use of degenerate modes and multiple resonant elements per unit cell. Finally, a topological phonon metamaterial based on a reduced-order model corresponding to a quantum spin Hall Hamiltonian showcases the full potential of the technique.

Metamaterial design

Our design approach starts by mapping the degrees of freedom from the target mass–spring model to DOFs in the metamaterial (plate modes in our elastic example). It continues by calculating a database characterizing the perturbation V introduced by different geometric elements (beams and holes in our case) using finite-element simulations. We then use the database to perform multiple combinatorial searches in different subspaces of the design space. This provides a good approximation of the metamaterial dynamics, since our perturbative design has been chosen so the first-order (linear) term of the Schrieffer–Wolff transformation provides an adequate description. We finally perform a gradient optimization on a design containing multiple unit cells, to cancel second-order effects arising from the interaction between different geometric elements. This gradient optimization leads to a highly accurate design if the nonlinearity is sufficiently small.

In our design examples, the mapping of metamaterial modes to the discrete model DOFs is the only heuristic step, although this could easily be automated. We note that all design examples presented here are numerical simulations using finite-element modelling. We model steel plates of size 10 mm × 10 mm × 0.5 mm, and epoxy resin beams of length 1 mm, thickness 0.5 mm, and width varying in the range 0.1–0.3 mm. Numerical details and the example mass–spring models are given in the Methods.

Phononic Veselago lens. We choose the classical Veselago lens[29] metamaterial as a first example, as it is a well-understood system that has been demonstrated in both optical[1] and phononic[5] platforms. In the phononic Veselago lens, a double-negative medium (that is, a

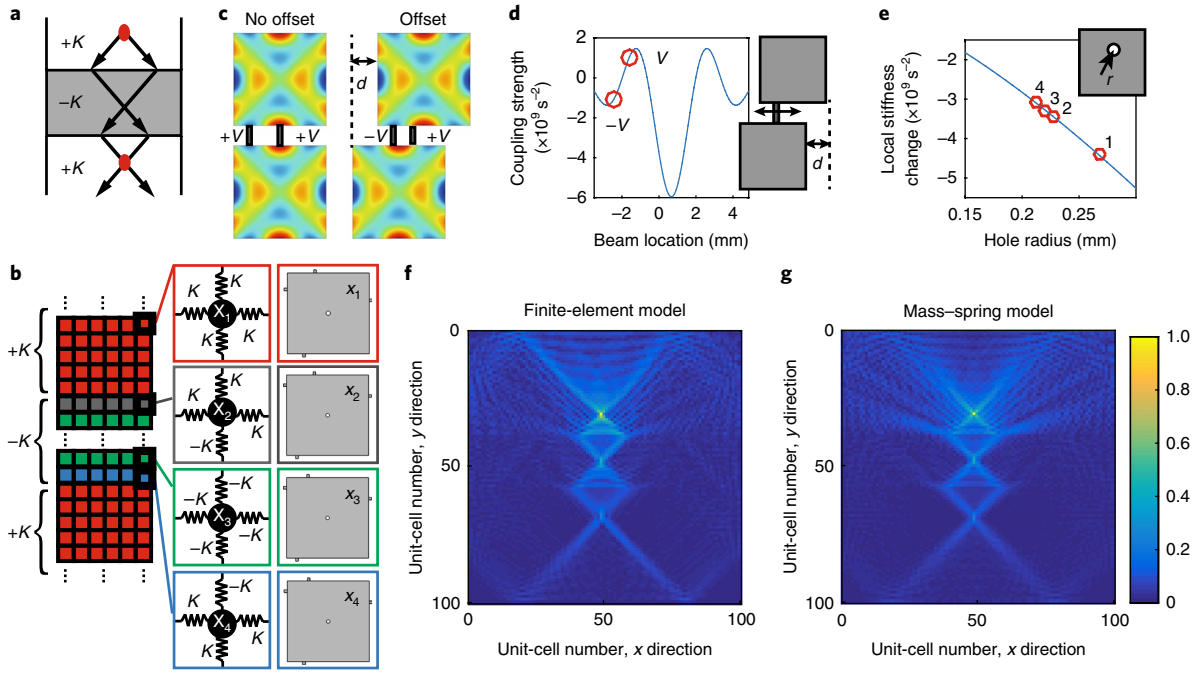

Fig. 2 | Veselago lens metamaterial example. a, A schematic of focusing in the Veselago lens. **b**, Mass–spring model of the lens, showing construction of the four different unit cells (a unit cell with all positive springs, a unit cell with all negative springs, and two interface unit cells with a combination of positive and negative springs), and the corresponding metamaterial unit cells. Lattice sites (x_1, x_2, x_3, x_4) are local resonators with their own mass and spring. The mass–spring model contains 100×100 unit cells, where the double-negative region consists of 19 unit cells in the centre. **c**, Illustration of the plate offset concept with mode 24: when plates are aligned (left), only couplings of one sign are possible. If plates are offset by distance d, both positive and negative couplings are possible. **d**, Calculated coupling stiffness for different beam locations at a given offset, where data points show locations of the beams to achieve positive and negatives stiffness. **e**, Calculated local stiffness change for different hole radii, where data points show the radii in each of the four unit cells for the intra-plate coupling compensations. **f**, Results for the metamaterial lens from finite-element simulations, at 175.284 kHz. **g**, Results for the mass–spring model lens, at 175.204 kHz. The colour bar applies to both **f** and **g**, and indicates the normalized amplitude of the r.m.s. displacement.

medium with negative effective modulus ($-K$) and negative effective density) is embedded in a conventional medium of equal but positive modulus ($+K$) and positive effective density (Fig. 2a). We create a mass–spring system that approximates the lens in a square lattice. The basic unit cell consists of a single resonator connected by springs to its four nearest neighbours (Fig. 2b).

We chose the 24th plate mode as our local DOF because this mode has a high enough stiffness compared with the beams and is well separated from neighbouring modes (Fig. 2b). Then we tabulate the perturbations of geometric elements by parameterizing the beam location, width (Supplementary Fig. 4) and offsets of the neighbouring plate (Fig. 2c) to calculate the desired couplings (Fig. 2d), and parameterizing the hole locations and radii to calculate the local frequency shift (Fig. 2e). We then perform the combinatorial searches on subspaces of individual geometric elements to yield the desired model (Fig. 2b). We finally perform a gradient optimization to reduce the error between the desired model and the metamaterial.

We analyse the resulting metamaterial lens using finite-element simulations (Methods). The results clearly illustrate the Veselago lens effect (Fig. 2f), where a planar inclusion of a doubly negative material leads to a perfect flat lens. Moreover, we show good agreement between finite-element simulations and the results of the mass–spring model (Fig. 2g).

Zero-group-velocity material. In the above example, we used one local mode per plate. We now demonstrate the mapping of multiple degenerate modes of a single plate to the DOFs of the discrete model by designing a zero-group-velocity (c_g) material. The zero-c_g material is analogous to a one-dimensional strip of a Lieb lattice[30], and is of interest as it is a perfectly periodic configuration with non-trivial couplings leading to a flat band. Such slow-wave states have been explored recently in photonic waveguides[31,32] and could have applications in sensing and information storage devices.

The zero-c_g lattice unit cell consists of three equal resonators in an 'L' configuration (Fig. 3a). In our target mass–spring model, we add an additional resonator not present in the original zero-c_g lattice, such that each vertical column in Fig. 3a can map to a pair of degenerate modes of a single plate (Fig. 3b). We chose the degenerate plate modes 21 and 22 (Fig. 3b). This selection is motivated by the following requirements: there is good separation between the degenerate pair of interest and neighbouring modes; and the mode profiles at the boundary exhibit a complex structure that enables us to achieve a wide variety of coupling stiffness. To prevent the additional resonator from influencing our desired dynamics, we shift its frequency outside our range of interest with the holes in the plate.

The simulated metamaterial dispersion matches the predictions of the objective mass–spring model (Fig. 3d), with only minor deviations from zero group velocity in the flat band arising from high-order long-range couplings (Supplementary Section 3 and Supplementary Fig. 5). This corroborates the ability of our method to engineer material performances.

Topological insulator. Topological insulators are electrically insulating in the bulk, yet conductive on the surface, and their surface states are immune to back-scattering and defects[33–35]. These materials have inspired a class of mechanical systems that mimic the functionality of topological insulators in the elastic domain[36–42]. Researchers have developed several analogies between topological spin–orbit systems and highly complex discrete mechanical

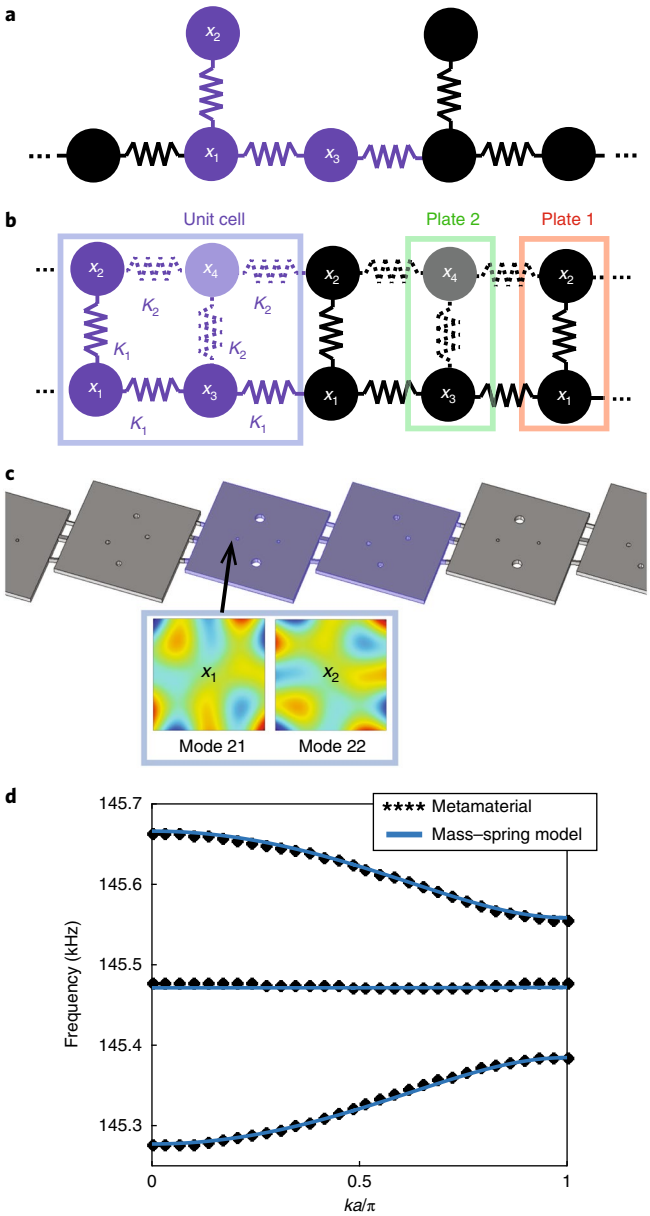

Fig. 3 | Zero-group-velocity metamaterial. a, The zero-c_g material mass–spring model. **b**, The mass–spring model used for metamaterial design, where each vertical column of two masses *x* and *y* represents two degenerate modes of one plate in the metamaterial. The metamaterial is optimized to separate mode y_2 in plate 2 from the other modes, and to push K_2 to 0. **c**, The design of the zero-c_g metamaterial, with the unit cell highlighted in purple, showing mode shapes 21 and 22 used in the design. **d**, The dispersion curves for the zero-c_g material mass–spring model compared with the designed metamaterial. Only the three energy bands of interest are shown for clarity.

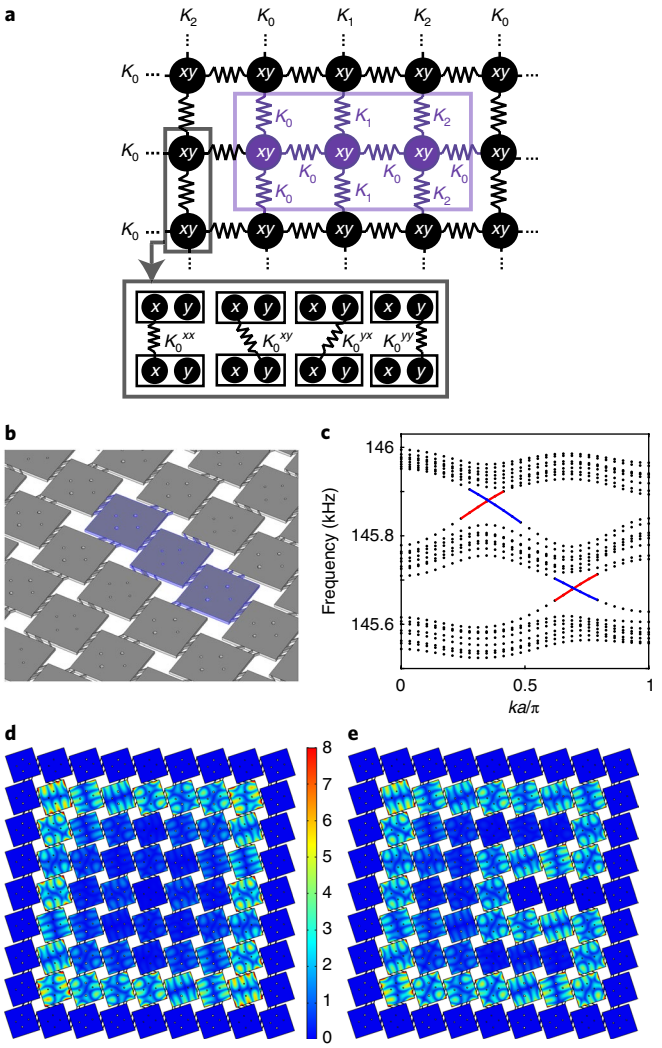

Fig. 4 | Topological insulator metamaterial. a, The mass–spring model and couplings for the topological insulator[36], where each mass *x* and *y* represents two degenerate modes of a plate in the metamaterial. The inset shows the construction of the couplings between neighbouring pairs of DOF *x* and *y*. **b**, The metamaterial designed from the topological insulator mass–spring model. **c**, The dispersion curves for the metamaterial, with one-dimensional periodicity, showing three bulk bands, indicated by the black points, separated by the two sets of counter-propagating edge modes, indicated by the red and blue solid lines. **d**, An example edge mode of the metamaterial. **e**, Edge mode propagation around a defect (three fixed plates) in the metamaterial. In **d** and **e**, the outer edge plates are fixed, and the colour bar indicates the amplitudes of both plots, in terms of total modal displacements with arbitrary normalized units.

lattices[36,43,44]. Here, we focus on the mass–spring model proposed in ref. [36], which contains six DOFs per unit cell (Fig. 4a). While this model was realized in a system of coupled pendula[36], each of which corresponds trivially to a discrete mass–spring resonator, the design of a metamaterial geometry implementing such a model remains an open research problem that our approach is able to solve.

This example highlights the ability of our method of using discrete models to design metamaterials. Properties such as topological phonons cannot be encoded using conventional algorithms: the topological invariants are quantized, which precludes the use of gradient methods, and their evaluation is extremely expensive, requiring the finite-element simulation of the material's dispersion relation at closely spaced wavenumbers for each individual geometric configuration. In contrast, a discrete tight-binding model, such as the one exploited here, can capture topological and other complex functionalities in a straightforward way.

The designed metamaterial translates each 2-DOF site into a single plate, utilizing the free plate modes 21 and 22 as degrees of freedom. Thus, the unit cell consists of three plates coupled with beams (Fig. 4b), whose locations and thickness are optimized to match the required stiffness matrices (Methods). We follow the same procedure as in the zero-group-velocity example. Due to the

higher complexity of the topological insulator discrete model, we allow the beams to be inclined (Fig. 4b) and use each beam angle as an additional fitting parameter. This increases the combinatorial search space and allows us to identify a suitable geometry.

The resulting metamaterial shows several distinctive features arising from the topologically non-trivial nature of the system's dynamics. First, the dispersion relation of a semi-infinite metamaterial stripe shows the characteristic pair of counter-propagating edge bands, crossing at $\pi/3$ and $2\pi/3$, in the gaps between the three bulk bands. Second, the normal modes of a finite material (containing 7×7 plates) show the presence of edge modes (Fig. 4d) that are in good agreement with the predictions of the target mass–spring model (Supplementary Section 4 and Supplementary Figs. 6 and 7). Finally, we demonstrate the topologically induced robustness of the edge modes against boundary defects, by simulating the same 7×7 finite system with three fixed plates obstructing the boundary mode (Fig. 4e). The edge mode persists despite the obstruction, highlighting the ability of topologically protected phonons to be used as defect-immune waveguides.

Advantages, limitations and outlook

The proposed method implements generic reduced-order, or tight-binding, models directly in complex metamaterials. This is accomplished by bringing concepts from quantum condensed matter to metamaterials, which enables the realization of various theoretical systems (such as exotic types of topological insulator). As tight-binding models can encode highly non-trivial phenomenology in a few very simple building blocks, using such models as a bridge between the desired phenomenology and a metamaterial's geometry provides a versatile tool[45] to engineer responses of metamaterials in various domains (such as mechanics, acoustics and photonics).

Our method complements other design tools[46–48] in that it can implement discrete models containing complex couplings (that is, multimodal, positive and negative). As such, it can realize functionalities (for example, topological protection) that are hard to capture in alternative paradigms such as homogenization[48]. It is applicable in generic platforms (mechanical, electromagnetic and photonic), as long as the weak coupling requirement is satisfied. This design method can be used in conjunction with other metamaterial analysis and design tools such as transformation optics[10,49], by utilizing transformation optics to determine the effective material properties required to manipulate an incident wave, and then our method to determine the metamaterial geometry necessary to achieve these properties.

The essential limitation of our method is its constraint to be implemented via weakly coupled unit cells. This means that our design approach cannot be used on platforms that are inherently strongly interacting. In addition, the requirement of weak interaction also results in narrowband effects. However, there are many applications that are compatible with such narrow bandwidth (for example, wireless communications, isolation and focusing of narrowband signals). Moreover, implemented for visible light with a base frequency of hundreds of terahertz, the weak-coupling constraints still allows for bandwidth in the terahertz regime. Another shortcoming of our method in its current form is the presence unaccounted resonances of the coupling elements (beams), which lead to retardation effects and limit the frequency of operation.

Further exploration should aim at increasing the available bandwidth and reducing constraints in the material parameters (for example, by accounting for beam retardation effects), deliberately introducing nonlinearity and providing experimental demonstrations in alternative platforms (electromagnetics[21,50] and photonics). Another direction of research opened by this work involves the development of reduced-order models implementing relevant functionalities (for example, filters, logic gates or photonic circuits with extreme computing capabilities[6]).

Methods

Methods, including statements of data availability and any associated accession codes and references, are available at https://doi.org/10.1038/s41563-017-0003-3.

Received: 7 November 2016; Accepted: 28 November 2017;
Published online: 15 January 2018

References

1. Pendry, J. B. Negative refraction makes a perfect lens. *Phys. Rev. Lett.* **85**, 3966–3969 (2000).
2. Grbic, A. & Eleftheriades, G. V. Overcoming the diffraction limit with a planar left-handed transmission-line lens. *Phys. Rev. Lett.* **92**, 117403 (2004).
3. Liu, Z., Lee, H., Xiong, Y., Sun, C. & Zhang, X. Far-field optical hyperlens magnifying sub-diffraction-limited objects. *Science* **315**, 1686 (2007).
4. Li, J., Fok, L., Yin, X., Bartal, G. & Zhang, X. Experimental demonstration of an acoustic magnifying hyperlens. *Nat. Mater.* **8**, 931–934 (2009).
5. Kaina, N., Lemoult, F., Fink, M. & Lerosey, G. Negative refractive index and acoustic superlens from multiple scattering in single negative metamaterials. *Nature* **525**, 77–81 (2015).
6. Silva, A. et al. Performing mathematical operations with metamaterials. *Science* **343**, 160–164 (2014).
7. Bückmann, T., Thiel, M., Kadic, M., Schittny, R. & Wegener, M. An elasto-mechanical unfeelability cloak made of pentamode metamaterials. *Nat. Commun.* **5**, 4130 (2014).
8. Schurig, D. et al. Metamaterial electromagnetic cloak at microwave frequencies. *Science* **314**, 977–980 (2006).
9. Tretyakov, S. *Analytical Modeling in Applied Electromagnetics* (Artech House, Boston, MA, USA, 2003).
10. Werner, D. H. & Kwon, D.-H. *Transformation Electromagnetics and Metamaterials: Fundamental Principles and Applications* (Springer, London, UK, 2014).
11. Sihvola, A. H. *Electromagnetic Mixing Formulas and Applications* (The Institution of Engineering and Technology, London, UK, 1999).
12. Gibson, W. C. *The Method of Moments in Electromagnetics* (Chapman and Hall/CRC, Boca Raton, FL, USA, 2007).
13. Hao, Y. & Mittra, R. *FDTD Modeling of Metamaterials: Theory and Applications* (Artech House, Boston, MA, USA, 2008).
14. Monk, P. *Finite Element Methods for Maxwell's Equations* (Clarendon Press, Oxford, UK, 2003).
15. Caloz, C. & Itoh, T. *Electromagnetic Metamaterials: Transmission Line Theory and Microwave Applications* (Wiley, Hoboken, NJ, USA, 2005).
16. Volakis, J. L., Sertel, K. & Usner, B. C. *Frequency Domain Hybrid Finite Element Methods for Electromagnetics* (Morgan & Claypool, San Rafael, CA, USA, 2006).
17. Reis, P. M., Jaeger, H. M. & van Hecke, M. Designer matter: a perspective. *Extrem. Mech. Lett.* **5**, 25–29 (2015).
18. Coulais, C., Teomy, E., de Reus, K., Shokef, Y. & van Hecke, M. Combinatorial design of textured mechanical metamaterials. *Nature* **535**, 529–532 (2016).
19. Kalinin, S. V., Sumpter, B. G. & Archibald, R. K. Big–deep–smart data in imaging for guiding materials design. *Nat. Mater.* **14**, 973–980 (2015).
20. Schumacher, C. et al. Microstructures to control elasticity in 3D printing. *ACM Trans. Graph.* **34**, 136 (2015).
21. Sun, Y., Edwards, B., Alù, A. & Engheta, N. Experimental realization of optical lumped nanocircuits at infrared wavelengths. *Nat. Mater.* **11**, 208–212 (2012).
22. Li, Y., Liberal, I., Giovampaola, C. D. & Engheta, N. Waveguide metatronics: lumped circuitry based on structural dispersion. *Sci. Adv.* **2**, e1501790 (2016).
23. Zhang, S., Xia, C. & Fang, N. Broadband acoustic cloak for ultrasound waves. *Phys. Rev. Lett.* **106**, 24301 (2011).
24. Schrieffer, J. R. & Wolff, P. A. Relation between the Anderson and Kondo Hamiltonians. *Phys. Rev.* **149**, 491–492 (1966).
25. Bravyi, S., DiVincenzo, D. P. & Loss, D. Schrieffer–Wolff transformation for quantum many-body systems. *Ann. Phys.* **326**, 2793–2826 (2011).
26. Winkler, R. *Spin–Orbit Coupling Effects in Two-Dimensional Electron and Hole Systems (Appendix B). Springer Tracts in Modern Physics*, Vol. 191 (Springer-Verlag, Berlin, Germany, 2003).
27. Wagner, M. *Unitary Transformations in Solid State Physics* (North Holland, Amsterdam, 1986).
28. Nemat-Nasser, S. & Srivastava, A. Negative effective dynamic mass-density and stiffness: Micro-architecture and phononic transport in periodic composites. *AIP Adv.* **1**, 1–10 (2011).
29. Veselago, V. G. The electrodynamics of substances with simultaneously negative values of ϵ and μ. *Sov. Phys. Uspekhi* **10**, 509–514 (1968).
30. Chalker, J. T., Pickles, T. S. & Shukla, P. Anderson localization in tight-binding models with flat bands. *Phys. Rev. B* **82**, 1–5 (2010).

31. Mukherjee, S. et al. Observation of a localized flat-band state in a photonic Lieb lattice. *Phys. Rev. Lett.* **114**, 245504 (2015).
32. Vicencio, R. A. et al. Observation of localized states in Lieb photonic lattices. *Phys. Rev. Lett.* **114**, 1–5 (2015).
33. Haldane, F. D. M. Model for a quantum Hall effect without Landau levels: Condensed-matter realization of the 'parity anomaly'. *Phys. Rev. Lett.* **61**, 2015–2018 (1988).
34. Hasan, M. Z. & Kane, C. L. Colloquium: Topological insulators. *Rev. Mod. Phys.* **82**, 3045–3067 (2010).
35. Qi, X.-L. & Zhang, S.-C. Topological insulators and superconductors. *Rev. Mod. Phys.* **83**, 1057–1110 (2011).
36. Susstrunk, R. & Huber, S. D. Observation of phononic helical edge states in a mechanical topological insulator. *Science* **349**, 47–50 (2015).
37. Nash, L. M. et al. Topological mechanics of gyroscopic metamaterials. *Proc. Natl Acad. Sci. USA* **112**, 14495–14500 (2015).
38. Wang, P., Lu, L. & Bertoldi, K. Topological phononic crystals with one-way elastic edge waves. *Phys. Rev. Lett.* **115**, 1–5 (2015).
39. Fleury, R., Sounas, D. L., Sieck, C. F., Haberman, M. R. & Alu, A. Sound isolation and giant linear nonreciprocity in a compact acoustic circulator. *Science* **343**, 516–519 (2014).
40. Mousavi, S. H., Khanikaev, A. B. & Wang, Z. Topologically protected elastic waves in phononic metamaterials. *Nat. Commun.* **6**, 19 (2015).
41. Khanikaev, A. B., Fleury, R., Mousavi, S. H. & Alù, A. Topologically robust sound propagation in an angular-momentum-biased graphene-like resonator lattice. *Nat. Commun.* **6**, 8260 (2015).
42. McHugh, S. Topological insulator realized with piezoelectric resonators. *Phys. Rev. Appl.* **6**, 14008 (2016).
43. Pal, R. K., Schaeffer, M. & Ruzzene, M. Helical edge states and topological phase transitions in phononic systems using bi-layered lattices. *J. Appl. Phys.* **119**, 84305 (2016).
44. Süsstrunk, R. & Huber, S. D. Classification of topological phonons in linear mechanical metamaterials. *Proc. Natl Acad. Sci. USA* **113**, E4767–E4775 (2016).
45. Serra-Garcia, M. et al. Observation of a phononic quadrupole topological insulator. *Nature* https://doi.org/10.1038/nature25156 (2018).
46. Lai, A. & Itoh, T. Composite right/left-handed transmission line metamaterials. *IEEE Microw. Mag.* **5**, 34–50 (2004).
47. Semouchkina, E. A., Semouchkin, G. B., Lanagan, M. & Randall, C. A. FDTD study of resonance processes in metamaterials. *IEEE Trans. Microw. Theory Tech.* **53**, 1477–1487 (2005).
48. Sihvola, A. Homogenization principles and effect of mixing on dielectric behavior. *Photon. Nanostruct.* **11**, 364–373 (2013).
49. La Spada, L. et al. Surface wave cloak from graded refractive index nanocomposites. *Sci. Rep.* **6**, 1–8 (2016).
50. Lin, Z., Pick, A., Lončar, M. & Rodriguez, A. W. Enhanced spontaneous emission at third-order Dirac exceptional points in inverse-designed photonic crystals. *Phys. Rev. Lett.* **117**, 107402 (2016).

Acknowledgements

This work was partially supported by the ETH Postdoctoral Fellowship to K.H.M., and by the Swiss National Science Foundation. The authors would like to thank R. Süsstrunk and O. Bilal for discussions.

Author contributions

K.H.M. and M.S.G. performed the optimization and simulation of the materials. K.H.M. wrote the manuscript. M.S.G. proposed the reduction approach and optimization algorithm. A.P. designed and performed the dynamic condensation. S.H. selected and interpreted the reduced-order models. C.D. provided guidance during all stages of the project. All authors contributed to the discussion and interpretation of the results, and to the editing of the manuscript.

Competing interests

The authors declare no competing financial interests.

Additional information

Supplementary information is available for this paper at https://doi.org/10.1038/s41563-017-0003-3.

Reprints and permissions information is available at www.nature.com/reprints.

Correspondence and requests for materials should be addressed to M.S.

Publisher's note: Springer Nature remains neutral with regard to jurisdictional claims in published maps and institutional affiliations.

Methods

The results presented in this paper have been calculated by using COMSOL Multiphysics for the finite-element simulations and MATLAB for the linear algebra calculations (except otherwise indicated). The two programs can communicate through the LiveLink interface provided by COMSOL. The simulations were performed in ETH Euler cluster nodes and accessed up to 400 GB of RAM.

In all simulations, we have used a linear elastic model with material parameters from epoxy resin for the beams (Young's modulus $E_B = 4.02$ GPa, Poisson ratio $\nu_B = 0.22$ and density $\rho_B = 1{,}190\ \mathrm{kg\,m^{-3}}$) and steel for the plates ($E_p = 193$ GPa, $\nu_p = 0.3$ and $\rho_p = 8{,}050$). We model steel plates of size 10 mm × 10 mm × 0.5 mm, and epoxy resin beams of length 1 mm, thickness 0.5 mm, and width varying in the range 0.1–0.3 mm.

Extracting the coupling matrix V from finite-element simulation. We extract the coupling matrices by calculating the first 80 eigenmodes for a system of two steel plates coupled by a single polymer beam. The eigenmodes are calculated using the COMSOL Multiphysics 3D linear elasticity solver, with a highly refined mesh containing 964,000 elements. This fine mesh is required since the frequency shift introduced by the beams is much smaller than the resonance frequency of the plates, and therefore small imprecisions in the plate eigenfrequencies result in large relative errors in the calculated coupling matrix.

We then sample the x, y and z components of each eigenmode's displacement. The sampling is done at 2,268 points at each plate, distributed over a test area extending 2 mm from the sides of the plate. The sampled displacements u for the 80 relevant eigenmodes are stored in a matrix, whose ith column $\mathbf{U}_j^i$ contains the x, y and z displacement for the ith eigenmode: $\mathbf{U}_j^i = \left(x_1^i, x_2^i, \ldots x_{2,268}^i, y_1^i, y_2^i, \ldots, y_{2,268}^i, z_1^i, z_2^i, \ldots, z_{2,268}^i\right)^T$. The subindex j is used to distinguish between the two plates.

We express the displacement of the coupled-plate system in terms of a basis containing the first 40 normal modes of a free plate. As our finite basis consists of a limited number of modes, it is incapable of exactly reproducing the coupled vibration profiles. For this reason, we use the Moore–Penrose pseudoinverse, which provides a least-square approximation to the mode profile. This approximation is given by $\mathbf{P}_j = (A^T A)^{-1} A^T \mathbf{U}_j$ where A is a matrix whose ith column contains the displacement of the ith free-plate eigenmode, sampled over the test area and organized in the same layout as U_j. We use 80 eigenmodes of the coupled system and 40 eigenmodes for the free plate. The mode selection must take into account several aspects: The number of eigenmodes for the two-plate coupled system should be twice the number of modes for the individual system, the coupled modes should not include any beam resonances, and families of degenerate modes should be either completely included or completely excluded. Once the matrix P_j has been calculated, we assemble the matrix:

$$P = \begin{pmatrix} P_1 \\ P_2 \end{pmatrix}$$

and calculate the coupling matrix as $V = PDP^{-1} - H_0$, where D is an 80×80 square matrix whose diagonal elements contain the eigenvalues of the coupled system, $D_{ij} = \left(2\pi f_i\right)^2 \delta_{ij}$, and H_0 contains the eigenvalues of an unperturbed single plate:

$$H_0 = \begin{pmatrix} D^0 & 0 \\ 0 & D^0 \end{pmatrix}$$

with $D_{ij}^0 = \left(2\pi f_i^0\right)^2 \delta_{ij}$ and f_i^0 being the ith eigenfrequency of an unperturbed plate.

The coupling matrix extraction method is equivalent to the first-order term of the Schrieffer–Wolff transformation, for a low-energy space spanning the first 40 eigenmodes of the unperturbed plate. This is because to first order, the Schrieffer–Wolff transformation is simply a restriction on the low-energy subspace, with the identity as a rotation matrix (Supplementary Section 1). Once this first-order transformation has been performed on a large low-energy subspace (spanning 40 local modes), we determine the effective theory for our 1–2-mode subspace by calculating a second Schrieffer–Wolff transformation approximated as a series expansion to an order between 1 and 4 (Supplementary Section 1).

Optimization process. *Objective models.* Here we describe the objective matrices V_T describing the design examples in the paper. For clarity, we use two separate coupling terms: V is the coupling between modes describing the actual metamaterial system, while V^T is the targeted coupling in the mass–spring model, whose functionality we seek to replicate. Our design approach seeks to adjust the metamaterial so V matches the desired V^T.

Phononic Veselago lens. The target coupling stiffness between unit cells is either $+K$ or $-K$. The effective masses are obtained by shifting the local resonance frequencies of the sites inside and outside the lens region. The normalized effective mass of a harmonic oscillator at a particular frequency is

$$M_{\mathrm{eff}}(\omega) = \left(1 - \frac{\omega_0^2}{\omega^2}\right)$$

where ω_0 is the resonance frequency of the mode and ω is the frequency of operation of the lens. The Veselago lens requires $M_{\mathrm{lens}}(\omega) = -M_{\mathrm{medium}}(\omega)$. The relation between the local resonance frequency of the sites inside and outside the lens region is thus $\omega_{\mathrm{lens}}^2 = 2\omega^2 - \omega_{\mathrm{medium}}^2$.

Zero-group-velocity material. The equation of motion of the system in Fig. 3b is $\ddot{\mathbf{u}}_i = V_{\mathrm{imod2}}^T \mathbf{u}_i + V_m^T \mathbf{u}_{(i+1)} + V_m^T \mathbf{u}_{(i-1)}$. The vector $\mathbf{u}_i$ contains the two DOFs x and y corresponding to the ith plate. The target matrices representing inter-plate couplings (V_m^T) and the local plate stiffness matrices (V_0^T, V_1^T) are

$$V_m^T = \begin{bmatrix} \alpha & 0 \\ 0 & 0 \end{bmatrix},\ V_1^T = \begin{bmatrix} \beta & \alpha \\ \alpha & \beta \end{bmatrix},\ V_0^T = \begin{bmatrix} \beta & 0 \\ 0 & \beta + \Delta \end{bmatrix}$$

where α is the coupling strength, β is the local stiffness of the plate, $\alpha << \beta$, and Δ is the frequency shift that separates the undesired additional mode introduced in the mapping stage.

We determine the plate offset, and thickness and position of the beams that best approximate the target coupling matrix V_m^T by performing a combinatorial search in the space of three-beam couplings. This is carried out by adding together the results from a pre-computed table of single-beam stiffness matrices corresponding to different beam locations and thicknesses. We then find the plate hole locations to satisfy the target matrices V_1^T and V_0^T using the same procedure. We finally perform a gradient-based optimization on a system containing multiple unit cells to reduce the second-order errors between the metamaterial and target stiffness (Supplementary Section 3).

Topological insulator. The mass–spring model unit cell for this topological insulator consists of three 2-DOF lattice sites[36] (Fig. 4a). The equation of motion is $\ddot{\mathbf{u}}_{ij} = V_{\mathrm{L}}^T \mathbf{u}_{ij} + V_0^T \mathbf{u}_{(i+1)j} + V_0^T \mathbf{u}_{(i-1)j} + V_{\mathrm{imod3}}^T \mathbf{u}_{i(j+1)} + V_{\mathrm{imod3}}^T \mathbf{u}_{i(j-1)}$. The vector $\mathbf{u}$ contains the two DOFs x and y, and i and j are the row and column indices of the unit cells in Fig. 4a. The target inter-plate coupling matrices are

$$V_n^T = \alpha \begin{bmatrix} \cos(2n/3) & \sin(2n/3) \\ -\sin(2n/3) & \cos(2n/3) \end{bmatrix}$$

where n is an integer that spans from 0 to 2. The intra-plate coupling matrix is $V_{\mathrm{L}}^T = I_2 \beta$, where I_2 is the 2×2 identity matrix, and β and α are as defined above.

Combinatorial optimization. We identify the optimal beam locations by performing an exhaustive search on combinations of beam locations and thicknesses. In this step, we calculate the coupling matrix V_{ij}^R for a system containing multiple inter-plate coupling beams by adding together the coupling matrices of systems containing a single coupling beam. The validity of this approximation is examined in Supplementary Section 2 and Supplementary Section 3.

We first run the optimization code for different plate offsets in the range between 2 mm and 4 mm, with a spacing of 0.2 mm. We then assemble a table of coupling matrices V_{ij} as a function of the beam location, for a fixed beam width of 0.2 mm. The coupling matrices are calculated using the finite-element method described in the coupling matrix extraction section. The coupling matrices corresponding to beam widths other than 0.2 mm are calculated assuming a linear relation between the beam width and the coupling matrix (that is, $V_{ij}(w) = [w/w_0] V_{ij}(w_0)$).

We then evaluate all combinations of beam locations (in steps of 0.1 mm) and beam widths (between 0.1 m and 0.5 mm in steps of 0.01 mm). We identify the optimal beam parameters by comparing the calculated coupling matrices with the objective coupling matrices. Before this comparison, the calculated and objective matrices V_{ij} are normalized using the Hilbert–Schmidt norm $|V| = \sqrt{\mathrm{Tr}[V^T V]}$. This is done because the exact norm can be adjusted after the fact by finely scaling the beam widths, and is enabled by the approximately linear relation between the beam width and the coupling matrix (Supplementary Section 2). In this step, we discard beam combinations whose norm is more than 50% off the target value, because those would result in extreme beam dimensions after rescaling.

The exhaustive search code is written in C++ to maximize its speed. For every offset (we considered ten of them), the code explores 10^9–10^{10} configurations and takes between 43 s and 197 s to run on a 2.5 GHz Intel Core i7 laptop.

Gradient optimization. The gradient optimization is performed after the exhaustive search, to refine the beam parameters and account for interactions between

the beams. At every gradient iteration, the coupling matrix is evaluated for a reference configuration and for small variations around this configuration. For systems containing three beams (the topological insulator and zero-dispersion material), the configuration is represented by a vector of the form $\mathbf{s}=(x_1, w_1, \theta_1, x_2, w_2, \theta_2, x_3, w_3, \theta_3)^T$, where x_i is the location of the ith beam, w_i is the ith beam width and θ_i is the ith beam angle. Different numbers of beams can be accommodated by adding or removing components. The coupling matrix V_{ij}^R is also expressed in vector form $\mathbf{v}=(V_{11}, V_{21}, V_{12}, V_{22})^T$. These definitions allow us to define a Jacobian matrix such as $\mathbf{v}(\mathbf{s}_0+\Delta\mathbf{s})\approx\mathbf{v}_0+J\Delta\mathbf{s}$ where the columns of J are calculated as $\mathbf{J}_i=v(\mathbf{s}_0+\mathbf{S}_i)-\mathbf{v}(\mathbf{s}_0)$, and S is a matrix where each column $\mathbf{S}_i$ represents a perturbation in the configuration vector's ith component. We use perturbations of 0.04 mm for the beam locations, 0.01 mm for the beam thickness and 2° for the beam angles. The coupling matrix vector $\mathbf{v}(\mathbf{s})$ is calculated using the coupling matrix extraction method described earlier.

The optimized state of the system after a gradient iteration is defined as $\mathbf{s}_1=\mathbf{s}_0+\alpha SJ^T(JJ^T)^{-1}\mathbf{e}-S\mathbf{k}$, where $\mathbf{e}$ is the error vector $\mathbf{e}=\mathbf{v}-\mathbf{v}_T$, $\mathbf{v}_T$ is the objective coupling matrix $\mathbf{K}$ expressed in vector form, α is a parameter controlling the gradient descent speed and k is a vector from the Jacobian's kernel; that is, $J\mathbf{k}=(0\ \ 0\ \ 0\ \ 0)^T$. The value of α is set to 0.4 at the beginning of the optimization process and then increased to 1 when the modulus of the error vector $\mathbf{e}$ falls below 5% of the modulus of the objective vector $\mathbf{v}_T$.

The kernel vector k does not affect the coupling matrix and is chosen to minimize participation of unwanted modes. We observe that the addition of $\mathbf{k}$ reduces these unwanted modes by 30 to 50%. We determine the direction of k by first defining a scalar value ε that quantifies the participation of unwanted modes. The vector $\mathbf{k}$ is then given by the projection of the gradient of ε into the kernel of J. The gradient of E is defined with respect to the changes in the geometry, so $\mathbf{k}=\gamma\wp_{\mathrm{Kern}(J)}\nabla_S E$, where $(\nabla_S E)=E(\mathbf{s}_0+\mathbf{S}_i)-\epsilon(\mathbf{s}_0)$, and $\wp_{\mathrm{Kern}(J)}$ is a projector into the kernel of J. The value of E is defined as $E=\sqrt{E_1^2+E_2^2+\ldots+E_n^2}$, where n is the number of coupled modes within our frequency range of interest, and $E_i=|\,(I-P)U_i^{\mathrm{FEM}}\,|$ is defined as the distance between the ith coupled mode's displacement profile in the test area $\mathbf{U}_i^{\mathrm{FEM}}=(x_1^i, x_2^i, \ldots x_{2,268}^i, y_1^i, y_2^i, \ldots, y_{2,268}^i, z_1^i, z_2^i, \ldots, z_{2,268}^i)^T$ and its projection into free-plate modes within the range of frequencies of interest, implemented with the projector $P=A(A^TA)^{-1}A^T$, where A is a vector whose columns contain the sampled displacements of the free-plate modes in the frequency range of interest, following the same layout as $\mathbf{U}_i^{\mathrm{FEM}}$. The errors in the two coupled plates are reduced to a single number E by taking the r.m.s. value of the two errors. The norm of k is adjusted empirically between 0.5 and 2.

Finite-element simulations. *Phononic Veselago lens.* Our model Veselago lens consists of 100 × 100 unit cells, each of them containing 141,000 elements. To solve this system, we follow a dynamic condensation approach[51]. We cut each unit cell halfway along the length of the beams and define a transfer matrix that relates the displacements and forces acting on the boundary DOFS at the connection points, using 117 DOFs for every connecting beam cross-section. We do this by first defining the unit-cell dynamic force-balance equation $-M\omega^2\mathbf{u}+ib\omega M\mathbf{u}+V\mathbf{u}=\mathbf{F}$, where M and V are the unit cell's mass and stiffness matrices obtained from COMSOL, and $b=33\ \mathrm{s}^{-2}$ is a damping parameter. We then introduce the dynamic stiffness matrix $D=-M\omega^2+ib\omega M+V$ and decompose the set of nodal forces and displacements into sets associated with boundary (b) and interior (i) nodes. By prescribing zero force at the interior nodes, the interior displacements can be condensed as $\mathbf{u}_i=-D_{ii}^{-1}(D_{ib}\mathbf{u}_b)$. As a result, we obtain a condensed matrix $D_{\mathrm{con}}=D_{bb}-D_{bi}(D_{ii}^{-1}D_{ib})$. We solve this system of equations using the PARDISO solver included in the Intel Math Kernel Library, which can solve systems with multiple right-hand sides without repeating common steps such as the matrix factorization. Similarly, we define a conversion matrix

$$C=\begin{bmatrix}-D_{ii}^{-1}D_{ib}\\ I\end{bmatrix},$$

which provides the values of the full displacement vector u as a function of the boundary DOF's $\mathbf{u}_B$, $\mathbf{u}=C\mathbf{u}_b$.

We then solve the force-balance problem for the full lens in terms of the boundary nodes. The force at each node is set to zero, except for those in the interface between $x=50$ $y=31$ and $x=50$ $y=32$, which are driven with unit strength. After solving for the displacements in each step, we calculate the r.m.s. amplitude of every unit cell by using the equation $u_{\mathrm{r.m.s.}}\propto\sqrt{E_T}$, where E_T is the total steady-state energy stored in a unit cell, calculated as $E_T=(1/2)\mathbf{u}_B^{\dagger}C^{\dagger}(\omega^2M+V)C\mathbf{u}_B$ where † denotes the Hermitian conjugate. Due to the size and sparsity of the resulting matrices, the full finite-element simulation of the Veselago lens utilizes a slightly reduced mesh resolution resulting in a shift of the local resonance frequency with respect to the discrete model, which has been obtained from a single-unit-cell simulation (see caption of Fig. 2f,g).

Zero-c_g metamaterial and topological insulator. The zero-group-velocity metamaterial is simulated in COMSOL using a unit cell subject to Floquet boundary conditions at half the beam's length, using 1.02 million elements per unit cell. For the topological insulator dispersion relation (Fig. 4c), we model four unit cells (3 × 1 plates) stacked in a column in the finite dimension, such that the modelled system consists of 12 × 1 plates coupled with beams. This simulation was performed using 901,000 elements. Fixed boundary conditions were applied on both ends of the beams of the finite dimension, and Floquet boundary conditions were applied in the other dimension. To determine the polarization of the edge modes around the crossing points, we calculate on which side of the model, in the finite dimension, the stored energy density is localized. The exact locations of the edge mode crossing points depend on which plate within the three-plate unit cell is connected to the fixed boundary. The finite-size topological insulator was simulated directly in COMSOL using 2.6 million elements.

Code availability. The codes used to generate the plots are available from the corresponding author upon reasonable request.

Data availability. The data that support the plots are available from the corresponding author upon reasonable request.

References

51. Petyt, M. *Introduction to Finite Element Vibration Analysis* (Cambridge University Press, New York, NY, USA, 2015).